https://doi.org/10.5194/egusphere-2026-5998
Preprint. Discussion started: 10 November 2026
© Author(s) 2026. CC BY 4.0 License.

Uncertainty-aware XCO_2 mapping over China through adaptive fusion of multi-source satellite observations

Hongxia Li[1], Qin He[1,*], Shuo Wang[2,3,*], Kai Qin[1], Jason Blake Cohen[1], Ye Feng[1], Honghui Gao[1], ZhengQiang Li[4], Yang Bai[5], and Lu Zhang[6]

[1]School of Environment and Spatial Informatics, China University of Mining and Technology, Xuzhou, 221116, China
[2]Jiangsu Key Laboratory of Coal-Based Greenhouse Gas Control and Utilization, China University of Mining and Technology, Xuzhou, 221116, China
[3]Carbon Neutrality Institute, China University of Mining and Technology, Xuzhou, 221116, China
[4]State Environment Protection Key Laboratory of Satellite Remote Sensing, Aerospace Information Research Institute, Chinese Academy of Sciences, Beijing, 100101, China
[5]College of Geography and Environmental Science, Henan University, Kaifeng, 475004, China
[6]National Satellite Meteorological Center (National Centre for Space Weather), China Meteorological Administration, Beijing, 100101, China

Correspondence to: Qin He (heqin@cumt.edu.cn) and Shuo Wang (wangshuo@cumt.edu.cn)

Abstract. Multi-source satellite observations of the column-averaged dry-air mole fraction of carbon dioxide (XCO_2) are limited by sparse orbital sampling, cross-platform footprint mismatch, and heterogeneous retrieval uncertainties, leading to substantial spatial discontinuities and uncertainty propagation errors in regional XCO_2 mapping. To address these limitations, we developed an adaptive fusion framework integrating physics-based Gaussian oversampling and Bayesian maximum entropy (PGO-BME) for uncertainty-aware monthly XCO_2 reconstruction over China. Monthly observations from DQ-1, OCO-2, OCO-3, and GOSAT collected between June 2022 and December 2024 were fused within the framework. In hold-out validation, the framework achieved an overall R^2 of 0.90 and an RMSE of 0.63 ppm, substantially outperforming conventional pixel-center and area-weighting approaches. Independent validation against the Total Carbon Column Observing Network (TCCON) further showed R^2 values of 0.93 at both the Hefei and Xianghe stations. The reconstructed dataset preserved both large-scale atmospheric transport patterns and localized anthropogenic enhancements, while posterior uncertainties were consistent with the corresponding spatial prediction errors. These results demonstrate that physically constrained, uncertainty-aware fusion can improve the spatial continuity and reliability of satellite XCO_2 fields while retaining atmospheric CO_2 variability across spatial scales.

1 Introduction

Since the Industrial Revolution, fossil fuel combustion and land-use change have driven a sustained increase in atmospheric CO_2 concentrations, further strengthening the need for accurate and continuous monitoring of regional atmospheric CO_2 distributions(Reichstein et al., 2013; Friedlingstein et al., 2025; Lu et al., 2025; Qin et al., 2023; Yuan et al., 2025; Xia et al., 2024). Satellite XCO_2 observations provide broad spatial information and serve as an essential observational constraint for regional carbon-cycle studies and carbon source-sink assessments(Byrne et al., 2023; Chen et al., 2025a). However, current

https://doi.org/10.5194/egusphere-2026-5998
Preprint. Discussion started: 10 November 2026
© Author(s) 2026. CC BY 4.0 License.

carbon satellite observations remain limited by sparse sampling, heterogeneous retrieval uncertainties, and differences in observational footprints and spatial response characteristics across platforms, resulting in substantial data gaps and difficulties in cross-scale matching(Zhang et al., 2024; Taylor et al., 2023; Eldering et al., 2019; Chen et al., 2025b). Meanwhile, the propagation of observation errors from different sources during multi-source fusion and continuous XCO_2 reconstruction remains insufficiently characterized(Lee et al., 2025; Wu et al., 2023; Wang et al., 2023). Therefore, developing a fusion strategy that incorporates both physical constraints and uncertainty representation is essential for constructing reliable and spatially continuous regional XCO_2 products.

Ground-based networks such as TCCON provide accurate and long-term XCO_2 measurements, but their sparse distribution limits spatially continuous monitoring(Laughner et al., 2024). Satellite remote sensing has extended CO_2 observations from early thermal-infrared retrievals to shortwave-infrared carbon missions and emerging spaceborne IPDA lidar systems(Pan et al., 2021; Kuai et al., 2010; Buchwitz et al., 2007). These advances have substantially improved large-scale monitoring of atmospheric CO_2 and the identification of emission sources(Dou et al., 2022; Crisp et al., 2017; Helliker et al., 2004). However, constrained by the inherent mechanisms of passive remote sensing, practical observations are frequently hindered by cloud cover, aerosol contamination, and insufficient illumination during nighttime or at high latitudes(Ehret et al., 2008; Oshchepkov et al., 2013; Shao et al., 2026; Xia et al., 2026). Even active remote sensing satellites, despite their all-day observation capabilities, struggle to achieve ideal cross-scale matching with ground-based stations due to their narrow swath widths(Han et al., 2018; Han et al., 2025). Consequently, less than 10% of daily satellite data typically meets the quality requirements for scientific analysis(Crisp et al., 2017). Such data scarcity and discontinuity severely undermine the reliability of flux inversions. Given the limited spatiotemporal coverage of single satellites, overcoming the inherent constraints of multi-source heterogeneous data is imperative. Constructing a high-precision, spatiotemporally seamless greenhouse gas concentration product to accurately assess its climate and environmental impacts has become a pressing scientific challenge in atmospheric remote sensing.

Enhancing the spatiotemporal continuity and resolution of greenhouse gas observations at regional and global scales is a crucial prerequisite for accurate carbon source and sink inversions. Currently, researchers primarily rely on geostatistical spatiotemporal interpolation and machine learning-based data fusion to mitigate the coverage limitations of single carbon satellites(Tadić et al., 2015; Tadić et al., 2017; Sheng et al., 2023; Wang, 2026; Zhang et al., 2022; Bao et al., 2026). However, when applied to sparse and non-stationary real-world remote sensing datasets, existing methods reveal theoretical limitations. Traditional Kriging methods, constrained by stationarity assumptions and linear frameworks, are prone to over-smoothing effects and struggle to accurately quantify the uncertainties inherent in multi-source observations(Hu et al., 2024). Conversely, machine learning models often lack the capability to capture local spatial heterogeneity. Employing globally unified network architectures in study areas with significant regional variations frequently degrades prediction accuracy(Li et al., 2024; Qin et al., 2024). More critically, the discrete footprints of GOSAT, the narrow swaths of OCO-2/3, and CAMS reanalysis data present inherent barriers in spatial resolution and observation geometry(Wang et al., 2022). Direct fusion inevitably encounters two core challenges: scale mismatch and error heterogeneity. Conventional geometric mosaicking or point-sampling

https://doi.org/10.5194/egusphere-2026-5998
Preprint. Discussion started: 10 November 2026
© Author(s) 2026. CC BY 4.0 License.

techniques largely ignore the actual physical response mechanisms of the sensors(Sun et al., 2018). Previous studies have demonstrated that forcibly applying spatial resampling for cross-scale matching without accounting for these physical responses can induce scaling errors of up to 40%(Sun et al., 2018; Inamdar et al., 2023; Inamdar et al., 2020).

To address scale mismatch, heterogeneous observational errors, and the loss of spatial gradients under sparse satellite coverage, this study proposes an adaptive PGO-BME fusion framework that integrates physical constraints with probabilistic inference. By combining physics-based oversampling with Bayesian maximum entropy, the framework provides a more reliable representation of sensor differences and associated uncertainties in multi-source satellite XCO_2 observations. It improves the spatial continuity and reliability of the fused XCO_2 field while preserving physically meaningful spatial gradients, thereby providing a new pathway for generating high-precision, seamless, and spatiotemporally continuous greenhouse gas products.

2 Data and materials

2.1 OCO XCO_2 Data

Launched by NASA in 2014, the Orbiting Carbon Observatory-2 (OCO-2) is a dedicated satellite mission designed for high-resolution monitoring of atmospheric XCO_2. It carries three high-resolution grating spectrometers that measure reflected sunlight in three spectral bands centered near 0.765, 1.61, and 2.06 μm, corresponding to the O_2 A-band and the weak and strong CO_2 absorption bands, respectively(Crisp et al., 2004). Measurements in these three spectral bands are used jointly to retrieve XCO_2.Each measurement frame contains eight parallel footprints, with an OCO-2 footprint size of approximately 1.29 km × 2.25 km and a narrow swath of approximately 10 km. OCO-2 follows a sun-synchronous near-polar orbit with a 16-day repeat cycle. In contrast, OCO-3, launched in May 2019, is mounted on the exterior of the International Space Station (ISS) and operates in a non-sun-synchronous orbit covering approximately 52° S to 52° N. Although its observation timing and sampling characteristics differ from those of OCO-2, OCO-3 provides broadly comparable spatial resolution and incorporates an agile pointing mirror assembly that enables additional observation modes, including Snapshot Area Mapping (SAM). Its nadir footprints are approximately 2 km × 2 km, with a nominal narrow-swath width of approximately 13 km.

This study utilizes bias-corrected XCO_2 products from OCO-2 (OCO2_L2_Lite_FP 11r) and OCO-3 (OCO3_L2_Lite_FP 11r), spanning from June 1, 2022, to December 31, 2024. The observations are stored in NetCDF-4 format as daily files. We extracted data covering China and implemented quality control using the xco2_quality_flag parameter. Only retrievals with a flag of 0 (indicating good quality) were selected for the fusion process(Wang et al., 2025). These datasets were obtained from the NASA Goddard Earth Sciences Data and Information Services Center (GES DISC) at https://disc.gsfc.nasa.gov/datasets.

2.2 GOSAT

Launched on 23 January 2009, the Greenhouse Gases Observing Satellite (GOSAT) is a joint project of the Ministry of the Environment (MOE), the National Institute for Environmental Studies (NIES), and the Japan Aerospace Exploration Agency

https://doi.org/10.5194/egusphere-2026-5998
Preprint. Discussion started: 10 November 2026
© Author(s) 2026. CC BY 4.0 License.

(JAXA), and was the world's first satellite designed specifically to monitor atmospheric CO_2 and CH_4 from space. GOSAT carries the Thermal And Near-infrared Sensor for carbon Observation–Fourier Transform Spectrometer (TANSO-FTS), which measures reflected and emitted infrared radiation for retrieving atmospheric CO_2 and CH_4 column abundances. TANSO-FTS employs a point-sampling observation strategy, with an instantaneous field of view corresponding to a circular footprint of approximately 10.5 km in diameter at nadir. GOSAT completes one orbit in approximately 100 min and has a 3-day repeat cycle.

This study uses the bias-corrected GOSAT TANSO-FTS shortwave-infrared (SWIR) Level 2 XCO_2 product (V03.05) distributed by NIES. The V03.05 product is the bias-corrected version of the FTS SWIR Level 2 product and is available through the GOSAT Data Archive Service (GDAS). The study period extends from 1 June 2022 to 31 December 2024. Observations over China were extracted, and quality control was performed using the totalPostScreeningResult parameter. Only retrievals with totalPostScreeningResult = 0 were retained for subsequent fusion.

2.3 DQ-1

Launched in April 2022, Daqi-1 (DQ-1), China's first atmospheric environment monitoring satellite, operates in a sun-synchronous orbit at an altitude of approximately 705 km(Cao et al., 2026). As the world's first satellite equipped with an active lidar for CO_2 detection, DQ-1 has profoundly expanded the physical and spatiotemporal dimensions of global greenhouse gas monitoring(Benoy et al., 2017). Its core payload, the Aerosol and Carbon Detection Lidar (ACDL), employs spaceborne Integrated Path Differential Absorption (IPDA) technology. By actively emitting two laser pulses at adjacent wavelengths—1572.024 nm (online) and 1572.085 nm (offline)—the instrument achieves high-precision atmospheric retrievals based on the differential absorption characteristics of surface echo signals. Furthermore, the ACDL features an exceptionally small nadir footprint of approximately 70 m in diameter. Unlike passive remote sensing satellites such as OCO-2 and GOSAT, DQ-1 operates independently of solar illumination. This enables all-day (day-and-night) continuous observation capabilities, effectively filling observational gaps regarding nighttime carbon emissions and high-latitude polar regions, while also facilitating valid CO_2 detection above cloud tops(Cheng et al., 2025). For data quality control, we strictly retained only valid observations with a high signal-to-noise ratio (SNR), rigorously filtering out retrievals flagged as "no signal," "low SNR," or "cloudy"(Han et al., 2024). In the PGO-BME framework, the quality-controlled DQ-1/ACDL XCO_2 observations were used as deterministic hard data. This treatment was adopted because DQ-1 provides active lidar measurements with a distinct and highly localized observational support. The characteristics and roles of the four satellite datasets are summarized in Table 1.

Table 1. Multi-source satellite XCO_2 observations incorporated into the PGO-BME fusion framework

Sensor	Product/version used in this study	Native footprint	Quality-control criterion	Study period	Role in BME fusion
OCO-2	OCO2_L2_Lite_FP 11r	1.29 km × 2.25 km each; swath width ≈ 10.6 km	xco2_quality_flag = 0	Jun 2022–Dec 2024	Soft data

https://doi.org/10.5194/egusphere-2026-5998
Preprint. Discussion started: 10 November 2026
© Author(s) 2026. CC BY 4.0 License.

Sensor	Product/version used in this study	Native footprint	Quality-control criterion	Study period	Role in BME fusion
OCO-3	OCO3_L2_Lite_FP 11r	1.29 km × 2.25 km; swath width ≈ 13 km	xco2_quality_flag = 0	Jun 2022–Dec 2024	Soft data
GOSAT	TANSO-FTS SWIR Level 2 (V03.05)	circular footprint ≈ 10.5 km diameter	totalPostScreeningResult = 0	Jun 2022–Dec 2024	Soft data
DQ-1	ACDL XCO_2 orbital observations	nadir footprint ≈ 70 m diameter	Valid high-SNR observations retained;	Jun 2022–Dec 2024	Hard data

Note: OCO-2 and OCO-3 are described in the manuscript as bias-corrected Level-2 Lite products, whereas the GOSAT V03.05 product is described as validated and bias-corrected using TCCON measurements. In the corrected fusion design, DQ-1 observations are used as deterministic hard data; OCO-2, OCO-3, and GOSAT observations are incorporated as soft data after PGO processing. TCCON measurements are reserved for independent validation and are not used as fusion inputs.

2.4 TCCON

Established in 2004, the Total Carbon Column Observing Network (TCCON) is a global ground-based network that measures column-averaged dry-air mole fractions of atmospheric trace gases, including CO_2. The network uses ground-based Fourier transform spectrometers (FTSs) to record direct solar absorption spectra in the near-infrared region, from which accurate and precise column-averaged abundances of CO_2, CH_4, N_2O, CO, and other atmospheric constituents are retrieved. With more than 30 current and former measurement sites worldwide, TCCON provides a widely used reference for validating satellite XCO_2 retrievals. TCCON XCO_2 measurements have demonstrated a precision better than approximately 0.25 %. Since its establishment, TCCON has released several major retrieval versions, including GGG2009, GGG2012, GGG2014, and GGG2020.

This study uses the GGG2020 data version for independent validation of the reconstructed XCO_2 fields over the period from 1 June 2022 to 31 December 2024. TCCON data are distributed in netCDF files for individual sites. The Hefei and Xianghe stations in China were selected for validation. The corresponding observations were obtained from the TCCON Data Archive, and the site-specific data records should be cited according to the TCCON data-use requirements.

2.5 PGO

The PGO method constructs a spatial matching model that represents the physical imaging processes and observation geometries of the sensors. Instead of relying on conventional point or polygon approximations, PGO performs spatial matching of CO_2 observations by representing each satellite observation as a continuous sensitivity distribution over the Earth's surface(De Graaf et al., 2016). This approach avoids the idealized assumption of uniform sensor sensitivity within the field of view (FOV)(Sihler et al., 2017). Instead, each observation footprint is characterized using a continuous spatial sensitivity distribution. Specifically, a two-dimensional (2-D) super-Gaussian spatial response function (SRF) is used to represent the

https://doi.org/10.5194/egusphere-2026-5998
Preprint. Discussion started: 10 November 2026
© Author(s) 2026. CC BY 4.0 License.

sensitivity distribution within the sensor's FOV(Sun et al., 2018; Jin et al., 2025). For a given observation footprint, the SRF is expressed as follows:

$$S(x,y) = exp\left[-\left(\left|\frac{x}{w_x}\right|^{k_1} + \left|\frac{y}{w_y}\right|^{k_2}\right)\right] \quad (1)$$

Here, x and y represent the orthogonal projection distances from the surface target point to the center of the satellite's FOV in the along-track and across-track directions, respectively. The shape exponents $k_1$and k_2 control the characteristics of the super-Gaussian distribution. In this study, these exponents were determined based on the hardware specifications and imaging mechanisms of the satellite sensors. Candidate response shapes were first defined according to sensor type. With the footprint full width at half maximum (FWHM) held constant, the performance of the PGO method was compared across different shape exponents. A pre-established holdout set of Level-2 (L2) observations was then used to assess concentration matching errors and changes in spatial gradients. Finally, the selected configuration was evaluated using an independent test dataset.The terms w_x and w_y are scale parameters related to the Full Width at Half Maximum (FWHM) in the along-track and across-track directions, respectively. Based on the aforementioned SRF, the effective weight of a target grid cell or block is determined by the sensitivity distribution of the observation pixels covering that area. Assuming the spatial response integral of observation pixel i over target area x serves as the weight $wg_{i,x}$, the oversampled mean $\bar{\Omega}_{x,t}$ for the target area within a specific time window t is calculated as follows:

$$\bar{\Omega}_{x,t} = \frac{\sum_t \sum_i wg_{i,x} \times \Omega_i}{\sum_t \sum_i wg_{i,x}} \quad (2)$$

Here, Ω_i denotes the retrieved XCO_2 (in ppm) for each valid satellite observation i whose footprint overlaps the target area x.

2.6 Bayesian maximum entropy (BME) fusion

BME is a spatiotemporal geostatistical framework that integrates heterogeneous observations and their associated uncertainties.(Christakos and Li, 1998; Gao et al., 2023). It enables spatiotemporal interpolation and fusion by converting observations of varying precision into probability density functions (PDFs), rather than relying on the single deterministic values typical of traditional geostatistics(Christakos, 1990). The BME method moves beyond the rigid assumptions of strict normality and linear unbiased estimation required by traditional Kriging for non-stationary fields(Jiang et al., 2022; He et al., 2020b). Instead, it partitions available information into a General Knowledge Base (G-KB), reflecting regional statistical characteristics (e.g., spatiotemporal means and covariance structures), and a Site-specific Knowledge Base (S-KB) containing localized observations. Based on observational error characteristics, site-specific data are further categorized into deterministic "hard data" and uncertain "soft data." By maximizing Shannon entropy subject to G-KB constraints, BME derives an unbiased prior PDF ($f_G(x)$)(He and Kolovos, 2018; He et al., 2020a), with the core functional optimization expressed as:

$$H[f_G] = -\int f_G(x)\, ln f_G(x)\, dx \quad (3)$$

The spatiotemporal dependence of XCO_2 within the G-KB was characterized using a single-exponential covariance model, expressed as follows:

https://doi.org/10.5194/egusphere-2026-5998
Preprint. Discussion started: 10 November 2026
© Author(s) 2026. CC BY 4.0 License.

$$C(d,\tau) = cexp(-\frac{3d}{a_s})\, exp(-\frac{3\tau}{a_t}) \quad (4)$$

where d is the spatial separation (km) and $\tau = |t - t'|$ is the nonnegative temporal lag (days) between observations; C is the partial sill (ppm²), while a_s and a_t are the spatial and temporal practical ranges, respectively. The factor of 3 follows the practical-range parameterization of the exponential model in Tang et al(Tang et al., 2016). Model parameters were estimated by least-squares fitting to the empirical spatiotemporal covariance of the study data. The resulting fitted parameters are summarized in Table 2.

Table 2. Parameters of the fitted single-exponential spatiotemporal covariance model for XCO_2.

Covariance model	Spatial range (km)	Temporal range (days)	Partial sill (ppm^2)
Single exponential	400	2	0.99

A joint spatiotemporal neighbourhood search was adopted, with a larger maximum number of hard observations than soft observations, to combine direct observational constraints with the uncertainty information represented by soft-data distributions.Following the acquisition of the prior distribution, BME integrates local hard data vectors x_{hard} and soft data vectors x_{soft} into the prior knowledge base. In this study, quality-controlled DQ-1/ACDL observations were incorporated as deterministic hard data, whereas OCO-2, OCO-3, and GOSAT retrievals were treated as soft data after PGO-based cross-scale representation. For the passive satellite retrievals, sensor-dependent observation support and retrieval uncertainties were expressed through probability density functions $f_S(x_{\text{soft}})$, allowing their uncertainty information to be assimilated within the BME framework.

$$f_K(x_k) = \frac{\int f_G(x_k, x_{\text{hard}}, x_{\text{soft}}) f_S(x_{\text{soft}}) dx_{\text{soft}}}{\iint f_G(x_k, x_{\text{hard}}, x_{\text{soft}}) f_S(x_{\text{soft}}) dx_{\text{soft}} dx_k} \quad (4)$$

Here, f_G represents the joint prior PDF encompassing both the estimation point and all incorporated observation sites.

2.7 The PGO-BME Framework

To address the pronounced heterogeneity in spatial resolution, observation geometry, and uncertainty characteristics among multi-source carbon-monitoring satellites, this study develops a coupled PGO-BME framework. The framework consists of two stages: physical-response matching and spatiotemporal probabilistic assimilation. In the physical-response matching stage, a two-dimensional super-Gaussian spatial response function is used to represent the spatial response and observation support of passive satellite retrievals from OCO-2, OCO-3, and GOSAT. In this framework, adaptive weighting occurs in the PGO stage, where the normalized weights for each target grid cell are determined by the spatial responses of the satellite footprints contributing to that cell.The resulting PGO-based estimates and their associated uncertainties are subsequently represented as soft-data distributions for BME assimilation. This approach addresses limitations associated with conventional geometric mosaicking by generating target-grid estimates weighted by spatial sensitivity factors while simultaneously propagating uncertainties associated with satellite retrievals and atmospheric transmission. In this way, discrete satellite observations are

https://doi.org/10.5194/egusphere-2026-5998
Preprint. Discussion started: 10 November 2026
© Author(s) 2026. CC BY 4.0 License.

transformed into continuous probability distributions, facilitating the transition from deterministic observations to probabilistic soft data within the Bayesian framework.

In this study, the PGO procedure is applied to passive satellite retrievals from OCO-2, OCO-3, and GOSAT to construct cross-scale representations for subsequent soft-data assimilation. Quality-controlled DQ-1/ACDL observations are retained as hard data in the BME framework and combined with the soft-data distributions generated by PGO. Regional spatiotemporal dependence structures are then used to construct the general knowledge base (G-KB). Bayesian inference is subsequently performed to jointly integrate the hard and soft data and generate posterior predictions. The posterior distribution provides both concentration estimates and associated uncertainty measures, with posterior standard deviations used to characterize spatial prediction uncertainty. This probabilistic formulation enables the integration of heterogeneous multi-source observations while preserving local spatial gradients in the reconstructed XCO_2 field. The overall PGO-BME workflow is illustrated in Fig. 1.

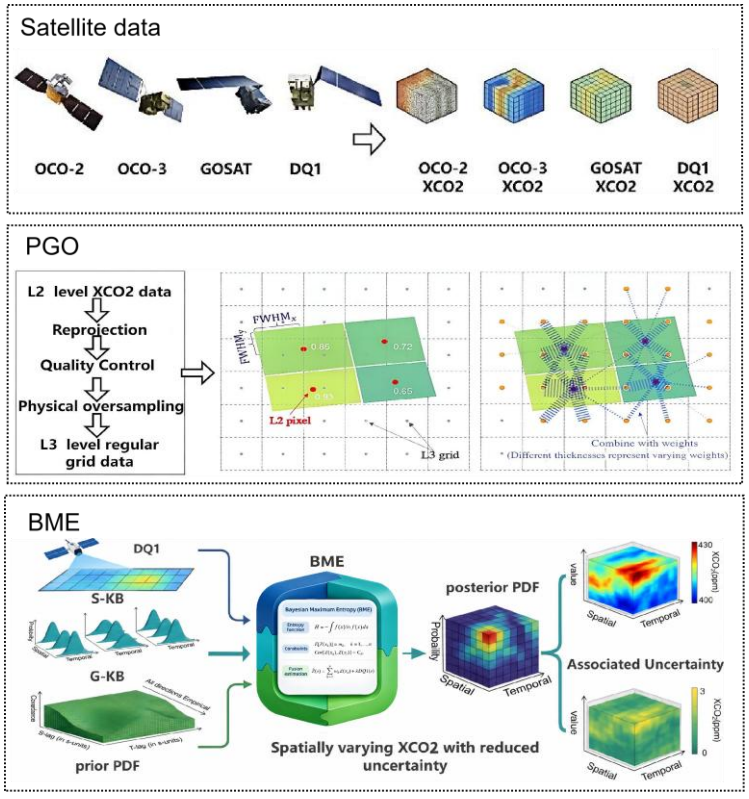


Figure 1. Workflow of the PGO-BME fusion framework for XCO_2 reconstruction over China.

2.8 Accuracy validation

To evaluate the spatial prediction performance of the PGO – BME framework under heterogeneous observational conditions, we employed a random hold-out validation strategy. After quality control,10 – 15 % of valid satellite retrievals were randomly

https://doi.org/10.5194/egusphere-2026-5998
Preprint. Discussion started: 10 November 2026
© Author(s) 2026. CC BY 4.0 License.

withheld at the individual-footprint level, before cross-scale matching and aggregation. This fraction was chosen to reserve samples for validation while retaining most of the available observations for fusion. Only the retained retrievals were used to construct the PGO grid-cell estimates and the associated soft-data distributions for BME.

Predicted means at the withheld observation locations were compared with the corresponding satellite retrievals.Predictive performance was quantified using the Pearson correlation coefficient (R),the coefficient of determination (R^2), the root mean square error (RMSE),and the mean absolute percentage error (MAPE).At the TCCON sites, posterior standard deviations were compared with the corresponding absolute prediction errors to assess whether larger estimated uncertainties were associated with larger errors.

3 Results and discussion

3.1 Hold-out validation performance of the three cross-scale fusion models

This study compares three fusion models employing different cross-scale matching strategies: pixel-center-based BME (POINT-BME), tessellation-based area-weighted BME (TES-BME), and PGO-BME. All three methods used the same set of retained satellite retrievals and the same BME settings. Fig.2 presents the hold-out validation results for the individual OCO-2 and OCO-3 datasets and for the combined dataset (Overall). The predicted values generally agree with the withheld satellite observations, with the scatter points concentrated around the 1:1 reference line.

Overall predictive performance improved as progressively more explicit representations of satellite observation support were introduced into the cross-scale matching process. The baseline POINT-BME model yielded an overall R^2 of 0.83, an RMSE of 0.79 ppm, and a MAPE of 0.13 %. Incorporating area weighting in TES-BME increased the overall R^2 to 0.86 and reduced the RMSE and MAPE to 0.68 ppm and 0.11 %, respectively. PGO-BME achieved the best overall hold-out validation performance, with an R^2 of 0.90, an RMSE of 0.63 ppm, and a MAPE of 0.10 %. These results indicate that explicitly representing the spatial response of satellite footprints can improve cross-scale matching under heterogeneous observation geometries.

The quantitative results summarized in Table 2 further demonstrate the performance differences among the three models. For OCO-2, PGO-BME achieved an R^2 of 0.89, an RMSE of 0.61 ppm, and a MAPE of 0.10 %, whereas the corresponding values for OCO-3 were 0.88, 0.66 ppm, and 0.11 %, respectively. Relative to POINT-BME, PGO-BME increased the overall R^2 by 0.07 and reduced the RMSE by 0.16 ppm. Relative to TES-BME, the overall R^2 increased by 0.04 and the RMSE decreased by 0.05 ppm. Given its superior overall validation performance and its explicit representation of satellite footprint responses, PGO-BME was adopted for the subsequent fusion of multi-source satellite XCO_2 observations.

https://doi.org/10.5194/egusphere-2026-5998
Preprint. Discussion started: 10 November 2026
© Author(s) 2026. CC BY 4.0 License.

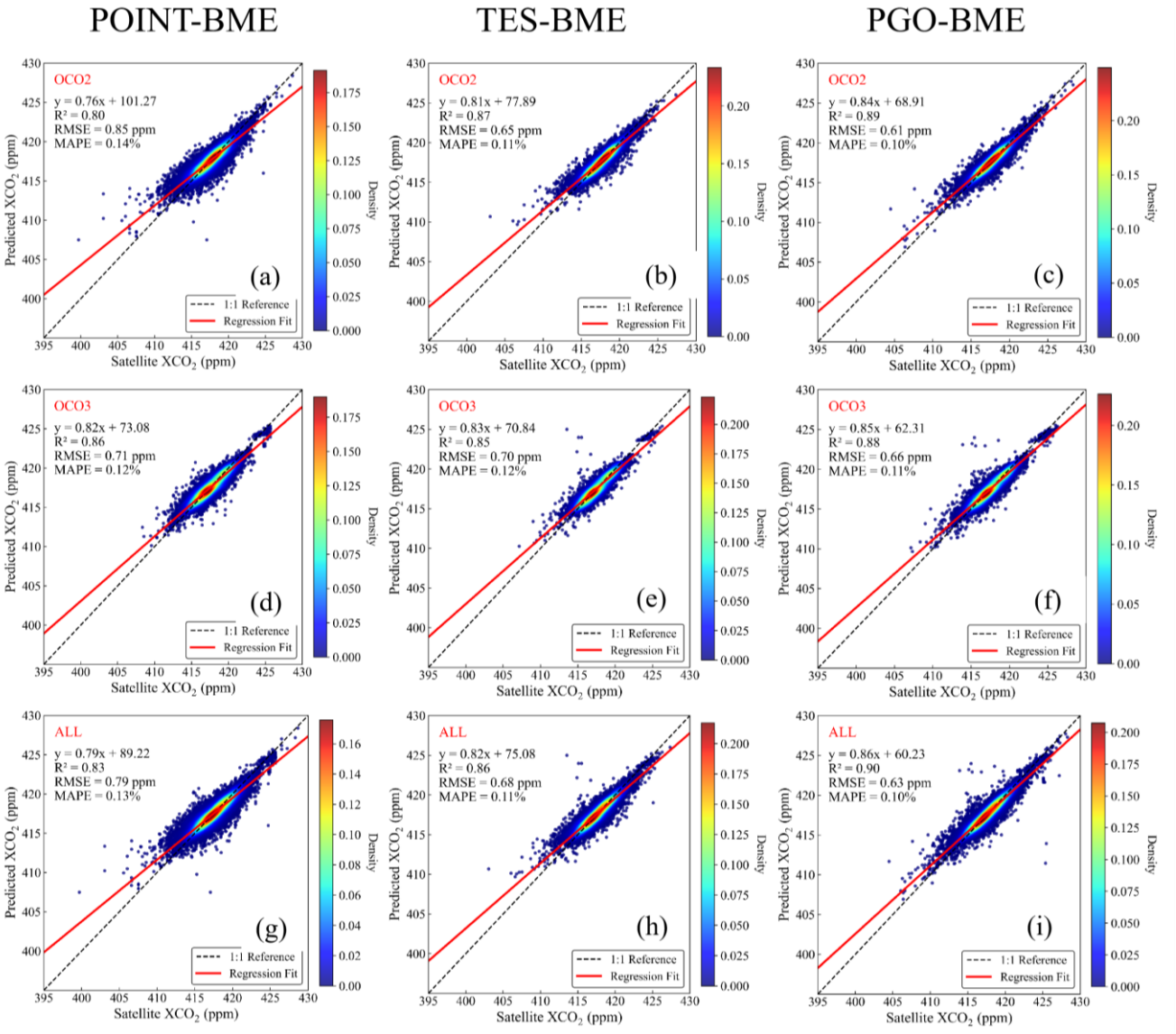


Figure 2. Scatter plots of hold-out validation results comparing predicted XCO_2 with withheld satellite observations. The panels are arranged by validation dataset across rows: (a–c) OCO-2, (d–f) OCO-3, and (g–i) the combined validation dataset (Overall); and by fusion model across columns: (a, d, g) POINT-BME, (b, e, h) TES-BME, and (c, f, i) PGO-BME.

https://doi.org/10.5194/egusphere-2026-5998
Preprint. Discussion started: 10 November 2026
© Author(s) 2026. CC BY 4.0 License.

Table 2. Hold-out validation performance of the three BME fusion models

Model	Dataset	R^2	RMSE (ppm)	MAPE (%)
POINT-BME	OCO-2	0.80	0.85	0.14
	OCO-3	0.86	0.71	0.12
	Overall	0.83	0.79	0.13
TES-BME	OCO-2	0.87	0.65	0.11
	OCO-3	0.85	0.70	0.12
	Overall	0.86	0.68	0.11
PGO-BME	OCO-2	0.89	0.61	0.10
	OCO-3	0.88	0.66	0.11
	Overall	0.90	0.63	0.10

Note: Bold blue values indicate the best performance per metric. R^2 higher is better; RMSE and MAPE lower is better. Overall refers to the combined OCO-2 and OCO-3 validation dataset.

3.2 Independent TCCON validation and assessment of posterior prediction uncertainty

To provide an external reference for evaluating the reconstructed XCO_2 fields, the CAMS reanalysis XCO_2 fields were first compared with independent TCCON observations at the Hefei and Xianghe stations (Fig. 3a–b). At Hefei, the CAMS fields yielded an R^2 of 0.86, an RMSE of 1.35 ppm, and a MAPE of 0.26 %. At Xianghe, the corresponding values were 0.87, 1.28 ppm, and 0.22 %, respectively. These results indicate that although the CAMS fields capture the overall variation in XCO_2, noticeable discrepancies remain relative to the ground-based TCCON observations.

The PGO-BME reconstructed XCO_2 fields were subsequently evaluated against the same TCCON observations (Fig. 3c–d). Improved agreement was observed at both stations. At Hefei, PGO-BME achieved an R^2 of 0.93, an RMSE of 0.78 ppm, and a MAPE of 0.12 %. At Xianghe, the corresponding values were 0.93, 0.97 ppm, and 0.15 %, respectively. Relative to CAMS, PGO-BME reduced the RMSE by 0.57 ppm at Hefei and by 0.31 ppm at Xianghe, while also increasing R^2 at both stations. These results demonstrate that the reconstructed fields provide closer agreement with independent ground-based XCO_2 observations than the CAMS reference fields.

The relationship between posterior prediction uncertainty and absolute prediction error was further examined at the two TCCON stations (Fig. 3e–f). At Hefei, the posterior standard deviation showed a positive correlation with the absolute prediction error (R = 0.81), indicating that larger posterior uncertainties generally correspond to larger prediction errors. A positive relationship was also observed at Xianghe (R = 0.64), although the association was weaker than at Hefei. Together, these results support the consistency between the spatial variation in posterior uncertainty and the magnitude of prediction

https://doi.org/10.5194/egusphere-2026-5998
Preprint. Discussion started: 10 November 2026
© Author(s) 2026. CC BY 4.0 License.

errors, suggesting that the posterior standard deviation provides useful information on the relative uncertainty of the reconstructed XCO_2 fields.

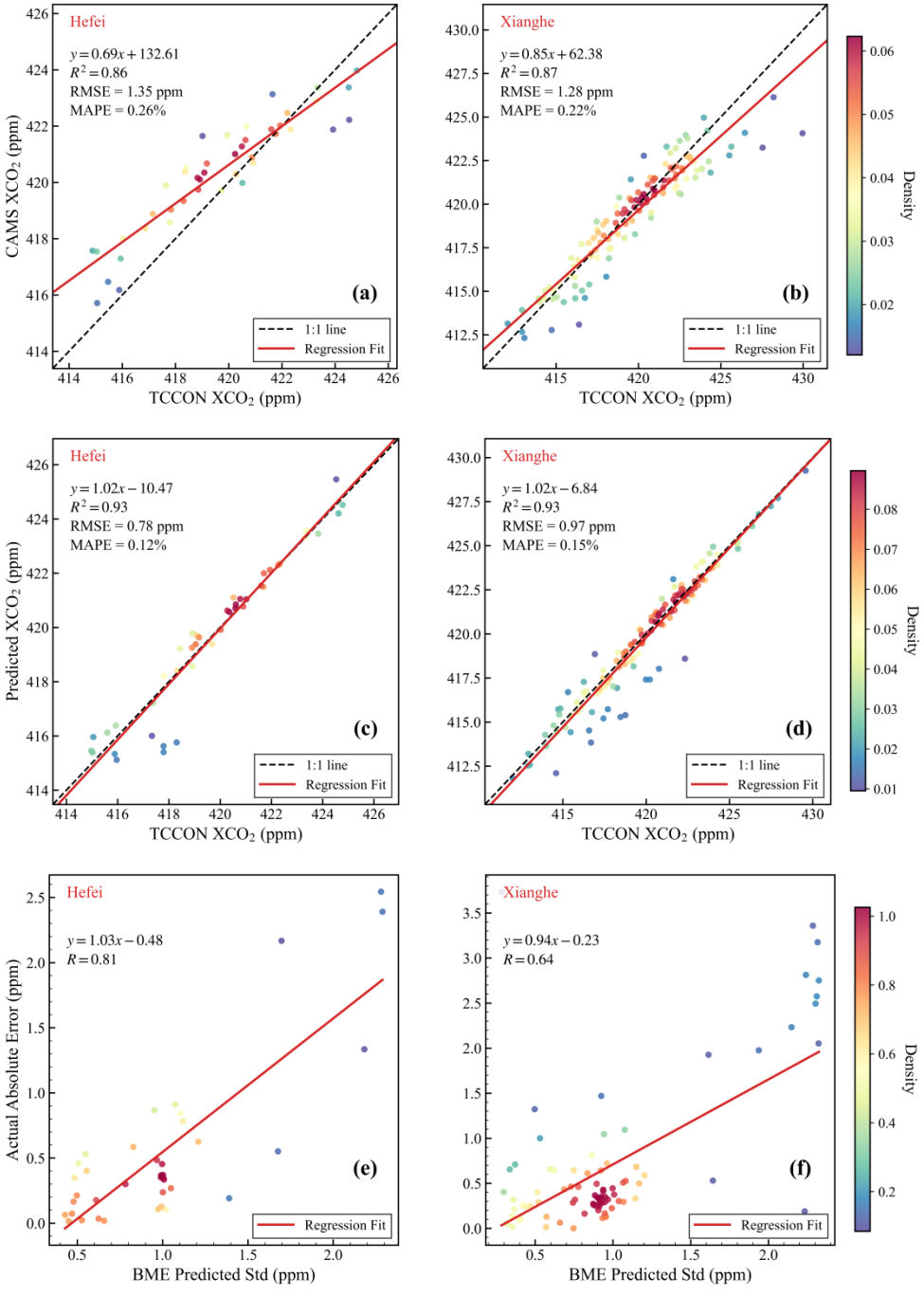


Figure 3. Independent TCCON validation and posterior uncertainty assessment. Scatter plots comparing CAMS XCO_2 fields with TCCON observations at (a) Hefei and (b) Xianghe, and PGO-BME reconstructed XCO_2 fields with TCCON observations at (c) Hefei and (d) Xianghe. Relationships between posterior standard deviation and absolute prediction error at (e) Hefei and (f) Xianghe.

https://doi.org/10.5194/egusphere-2026-5998
Preprint. Discussion started: 10 November 2026
© Author(s) 2026. CC BY 4.0 License.

3.3 Spatiotemporal evolution and uncertainty characteristics of XCO_2 over China

Fig. 4 presents a time-series comparison between daily mean TCCON measurements and PGO-BME reconstructed XCO_2 at the Hefei and Xianghe stations from June 2022 to December 2024. Overall, the reconstructed XCO_2 series agree well with the TCCON observations and reproduce the major seasonal variations and shorter-term concentration fluctuations at both stations. The differences between the reconstructed and observed values remain relatively small during most periods, although larger discrepancies occur during several intervals. The posterior uncertainty envelopes provide additional information on temporal variations in prediction uncertainty. Together with the independent validation results in Fig. 3, the time-series comparison provides further evidence for the temporal consistency of the PGO-BME reconstruction with independent ground-based observations over the study period.

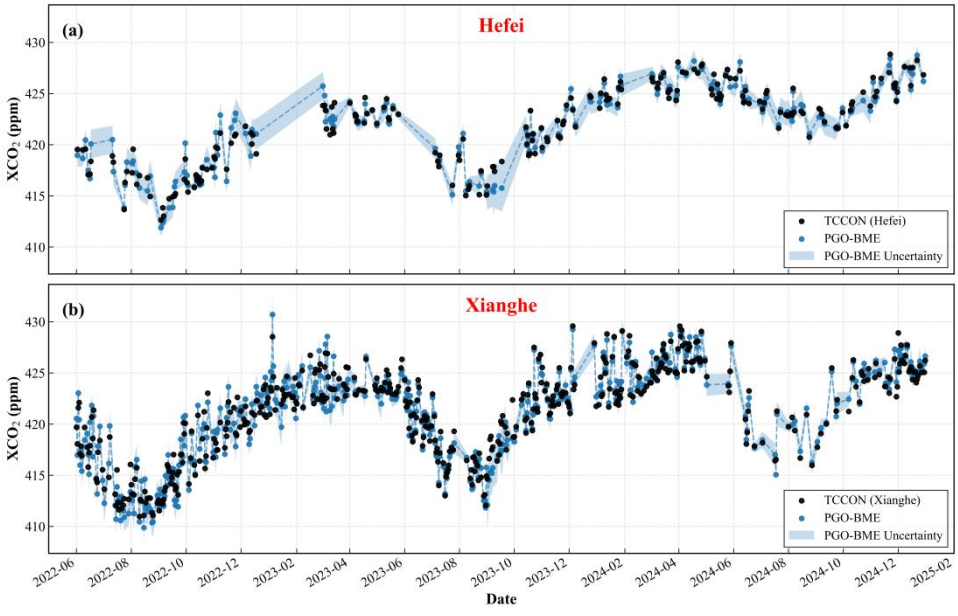


Figure 4. Time-series comparison of daily mean TCCON observations and PGO-BME reconstructed XCO_2 from June 2022 to December 2024 at (a) Hefei and (b) Xianghe. Blue shading represents the posterior uncertainty of the PGO-BME reconstruction.

Fig. 5 illustrates the spatial distributions of XCO_2 over China during four representative months: June, September, and December 2022 and March 2023. Owing to the sampling characteristics of the satellite observations and the availability of valid retrievals, the original observations (Fig. 5a–d) exhibit pronounced spatial sparsity and discontinuity, with substantial data gaps in several regions. After PGO-BME fusion, the reconstructed fields (Fig. 5e–h) provide spatially continuous XCO_2 coverage over the study domain. In addition to reproducing the broad spatial distribution apparent in the original observations, the reconstructed fields retain localized spatial gradients and regional heterogeneity. These characteristics facilitate the identification of localized XCO_2 enhancements that are difficult to resolve from sparse individual satellite observations.

The reconstructed XCO_2 fields also exhibit clear differences among the four representative months. Higher XCO_2 values are evident in March 2023, whereas lower concentrations occur over many regions in June and September 2022. This contrast is broadly consistent with the seasonal influence of terrestrial carbon uptake, with enhanced vegetation activity during the growing season contributing to lower atmospheric CO_2 concentrations.(Liu et al., 2026). Spatially, relatively high XCO_2 values occur over several densely populated and industrialized regions of eastern and central China, including the Beijing–Tianjin–Hebei region and the Yangtze River Delta. These regional enhancements are consistent with the combined influence of

https://doi.org/10.5194/egusphere-2026-5998
Preprint. Discussion started: 10 November 2026
© Author(s) 2026. CC BY 4.0 License.

atmospheric transport, terrestrial carbon exchange, and anthropogenic emissions; however, attribution to individual processes requires additional source and transport information.

The posterior uncertainty distributions (Fig. 5i–l) exhibit clear spatial variability associated with the availability of satellite observations. Regions with denser observational support generally show lower posterior uncertainties, with values below approximately 1.5 ppm in many well-observed areas, whereas sparsely sampled regions exhibit larger uncertainties, locally approaching 2.5 ppm. This spatial correspondence indicates that the PGO-BME framework adapts its posterior uncertainty estimates to variations in observational support. The resulting uncertainty fields therefore provide spatially explicit information on the relative reliability of the reconstructed XCO_2 estimates.

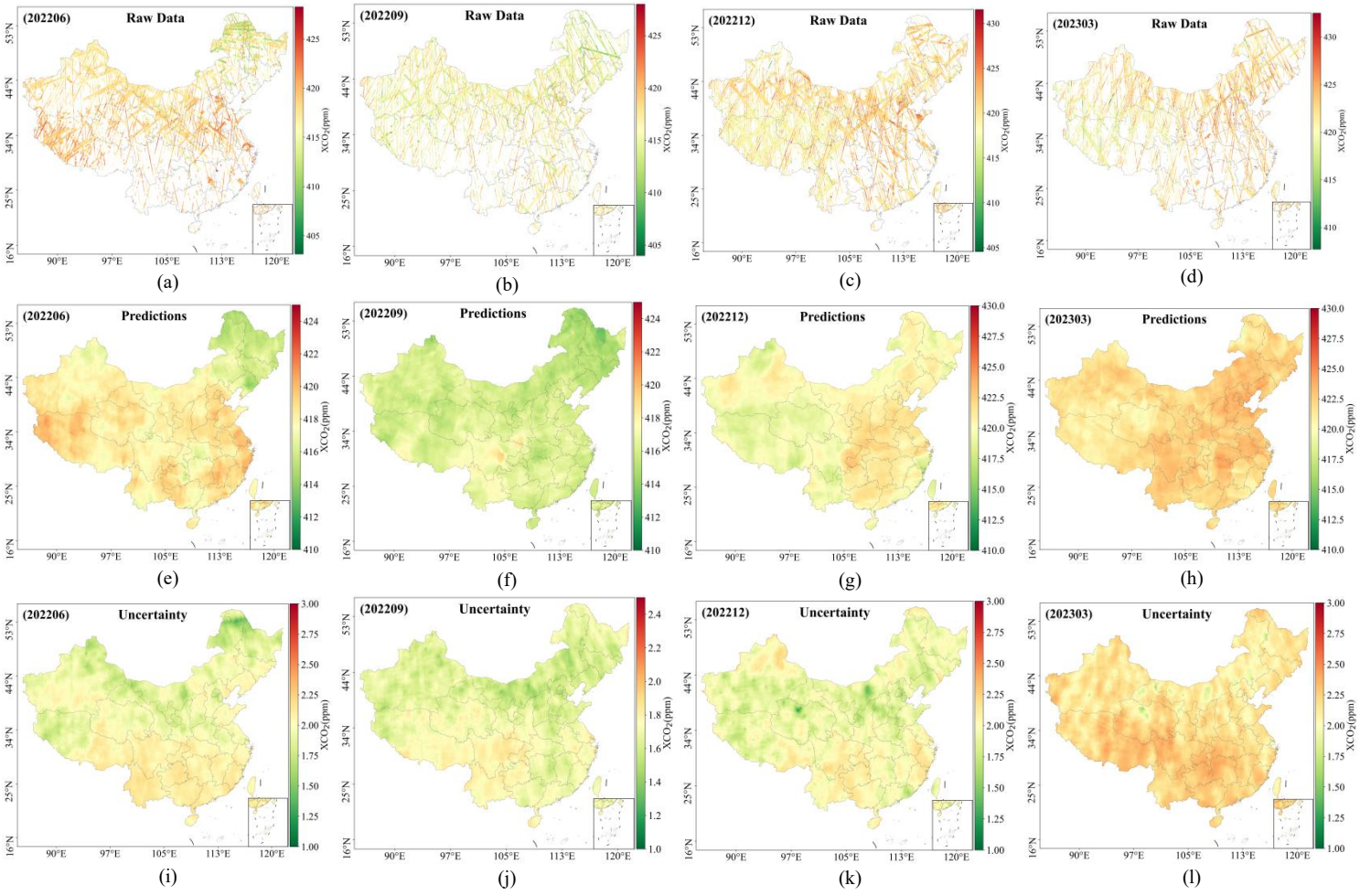


Figure 5. Spatial distributions of XCO_2 over China in June, September, and December 2022 and March 2023. The panels show (a–d) the original satellite observations, (e–h) the XCO_2 fields reconstructed using PGO-BME, and (i–l) the corresponding posterior uncertainties.

3.4 Structural consistency between PGO-BME reconstructed XCO_2 and CAMS reference fields

To evaluate the spatial structural consistency of the fused products, the Structural Similarity Index (SSIM) was calculated between the PGO-BME XCO_2 fields and the corresponding CAMS background fields for June, September, and December 2022, and March 2023 (Fig. 6). The SSIM values were 0.83, 0.64, 0.87, and 0.82, respectively, with a mean value of 0.79. The

https://doi.org/10.5194/egusphere-2026-5998
Preprint. Discussion started: 10 November 2026
© Author(s) 2026. CC BY 4.0 License.

relatively high SSIM values in June, December, and March indicate that the fused products preserved the broad spatial patterns represented by CAMS during these periods. In contrast, the lower SSIM in September suggests weaker structural agreement, which may be related to reduced valid satellite retrievals under cloud-affected conditions and the increased influence of reconstruction in data-sparse regions. December exhibited the highest SSIM, indicating the strongest spatial consistency between the PGO-BME product and the CAMS background field among the selected months. Overall, the results show that PGO-BME generally maintains the large-scale spatial structure of XCO_2 represented by CAMS, although the agreement varies seasonally with observational coverage. As CAMS is used as a background reference rather than independent ground truth, SSIM is interpreted here as an indicator of spatial structural consistency rather than direct evidence of reconstruction accuracy or physical authenticity.

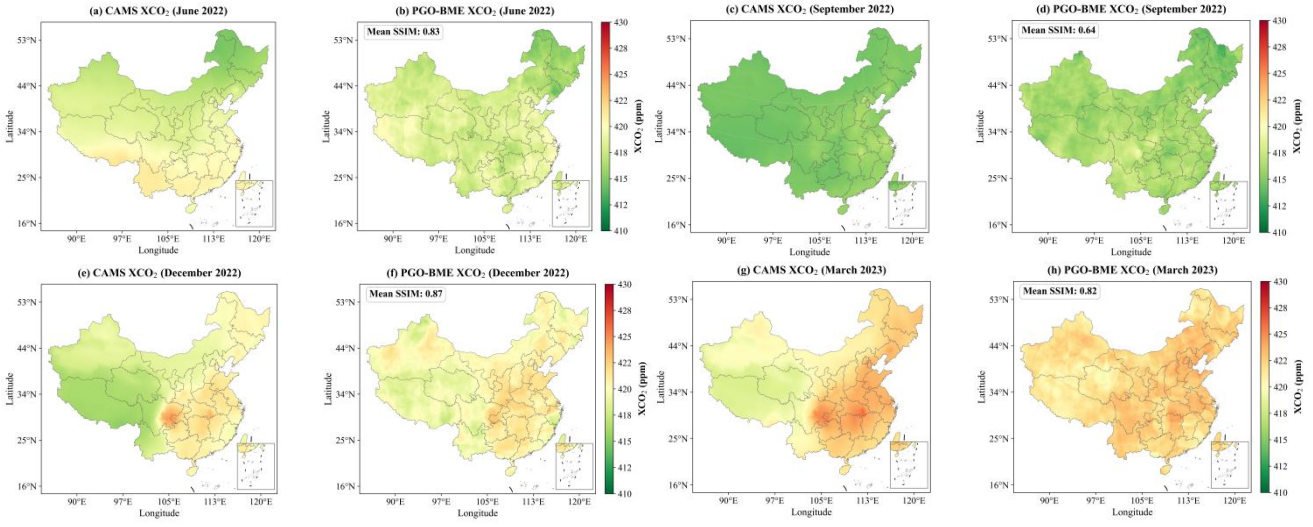


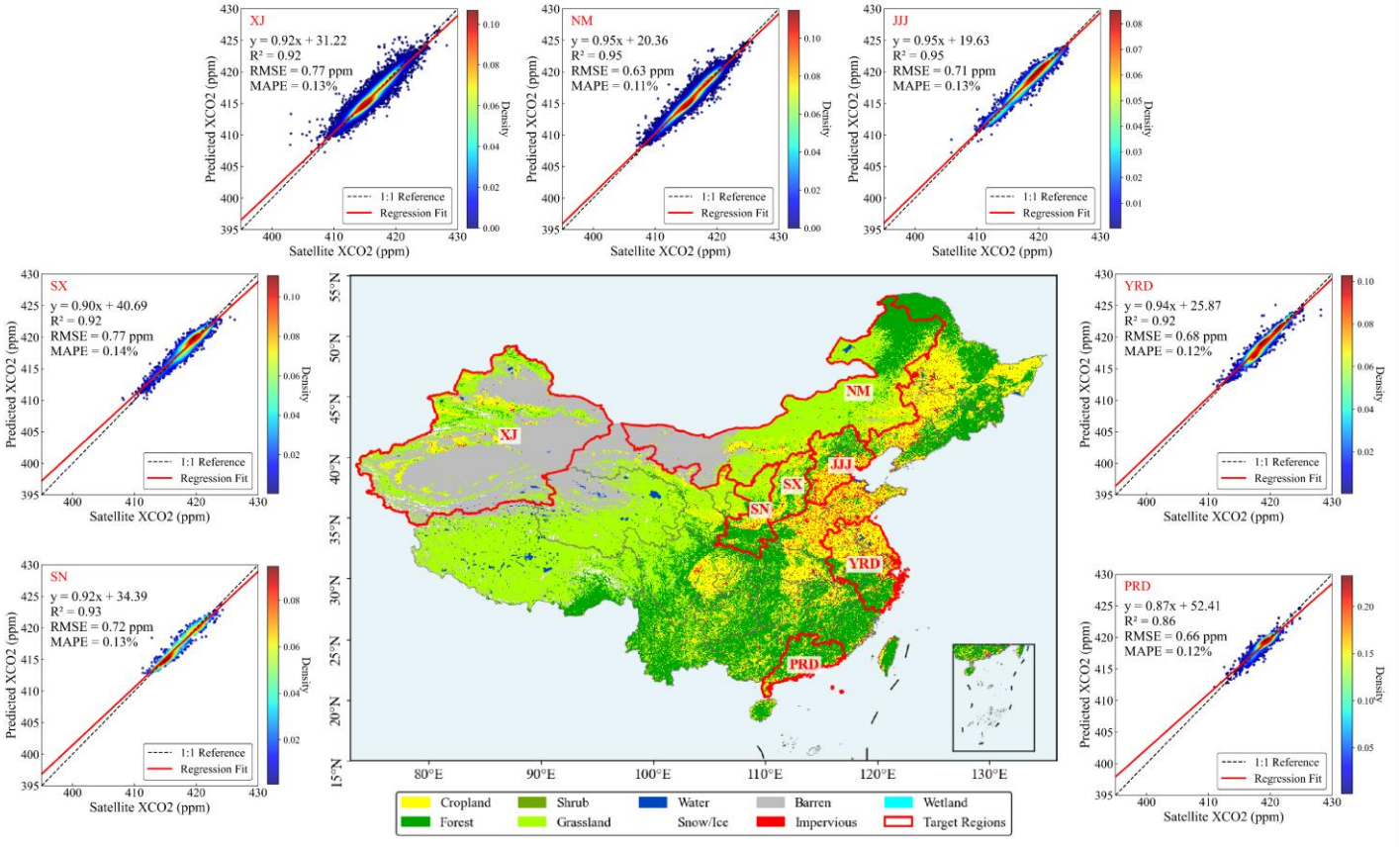
Figure 6. Spatial structural consistency between the PGO-BME reconstructed XCO_2 fields and the corresponding CAMS reference fields over China in June, September, and December 2022 and March 2023. The SSIM values shown in the PGO-BME panels indicate the degree of spatial structural agreement with the corresponding CAMS fields.

3.5 Regional hold-out validation against OCO-2 observations

Fig. 7 illustrates the cross-validation results between the PGO-BME fused products and the raw OCO-2 satellite observations across seven typical regions in China. Overall, the fused products exhibit robust quantitative accuracy across diverse regions and land cover conditions. The seven validation regions achieved an average R^2 of 0.92 and an average RMSE of 0.71 ppm, demonstrating the strong spatial generalization capability and low systematic estimation bias of the PGO-BME framework. Among the validation regions, the Beijing-Tianjin-Hebei urban agglomeration (JJJ) and Inner Mongolia (NM) yielded the most outstanding reconstruction accuracies, with R^2 values reaching 0.95 and 0.95, RMSEs of 0.71 ppm and 0.63 ppm, and MAPEs both below 0.14%, respectively. Inner Mongolia, dominated by grassland and barren land cover types, is characterized by strong spatial homogeneity of the underlying surface, low frequency of effective cloud cover, and excellent temporal continuity of satellite observations, thereby providing favourable conditions for high-precision reconstruction. Although the

https://doi.org/10.5194/egusphere-2026-5998
Preprint. Discussion started: 10 November 2026
© Author(s) 2026. CC BY 4.0 License.

JJJ region exhibits significant underlying surface heterogeneity—primarily consisting of impervious surfaces and croplands—the high frequency and density of valid satellite observation samples in this area ensure the model's precise capability to capture spatial gradient variations of XCO_2. The reconstruction accuracies for Shanxi (SX), Shaanxi (SN), Xinjiang (XJ), and the Yangtze River Delta (YRD) remained at consistently high levels, with R^2 values ranging from 0.92 to 0.93 and RMSEs between 0.68 and 0.77 ppm. These regions encompass diverse land cover patterns, transitioning from northwestern arid deserts to eastern coastal wetlands. This validates the model's reconstruction robustness under the complex topography of the Loess Plateau and varied vegetation conditions, including shrubs and forests. The Pearl River Delta (PRD) region exhibited relatively lower quantitative accuracy ($R^2 = 0.86$, RMSE = 0.66 ppm, MAPE = 0.12%). This is primarily because the PRD region features highly fragmented land cover, with forests, impervious surfaces, and water bodies spatially intertwined. Concurrently, this area is perennially affected by frequent cloud cover and high aerosol optical depth (AOD), leading to a significantly reduced acquisition rate of valid satellite observations and thus compounding the difficulty of fine-scale local reconstruction. Nevertheless, the RMSE for all validation regions remained below 0.8 ppm, comprehensively verifying the overall applicability and reliability of the PGO-BME fusion framework when confronting multi-source heterogeneous satellite data and complex surface environments.



https://doi.org/10.5194/egusphere-2026-5998
Preprint. Discussion started: 10 November 2026
© Author(s) 2026. CC BY 4.0 License.

Figure 7. Regional hold-out validation of the PGO-BME reconstructed XCO_2 fields against withheld OCO-2 observations across seven representative regions in China.

4 Conclusion

This study developed a PGO-BME framework for the reconstruction of spatially continuous XCO_2 fields over China using multi-source satellite observations from DQ-1, OCO-2, OCO-3, and GOSAT from June 2022 to December 2024. The framework combines physics-based cross-scale matching with probabilistic propagation of heterogeneous observational uncertainties. In contrast to point-center matching and area-weighted matching, PGO represents satellite observations according to their spatial response characteristics, while BME incorporates observation uncertainty through posterior estimation.

The model comparison demonstrates that PGO-BME achieved the best overall predictive performance in the fusion of multi-source satellite observations. For the combined OCO-2/OCO-3 validation dataset, PGO-BME yielded the highest R^2 (0.90) and the lowest RMSE (0.63 ppm) among the three models, while maintaining a low MAPE of 0.10%. Compared with POINT-BME, PGO-BME increased R^2 by 0.07 and reduced RMSE by 0.16 ppm. Building on the improvement already achieved by TES-BME, PGO-BME further increased R^2 by 0.04 and reduced RMSE by 0.05 ppm. These results indicate that physically informed cross-scale matching based on sensor spatial response characteristics can further improve the agreement between fused XCO_2 estimates and satellite observations, thereby enhancing the overall reconstruction performance.

The reconstructed products provided spatially continuous representations of XCO_2 over China and captured the major seasonal and regional patterns observed during the study period. Representative monthly maps showed higher XCO_2 levels during winter and spring and lower levels during summer and autumn. Localized XCO_2 enhancements were apparent in several eastern and central Chinese regions, including the JJJ and YRD areas. Relative to CAMS background fields, the PGO-BME products yielded SSIM values of 0.83, 0.64, 0.87, and 0.82 for June, September, and December 2022 and March 2023, respectively. These results indicate that the reconstructed fields generally retained the broad spatial structures represented by CAMS, although the level of agreement varied among the selected months. The improved spatial continuity, together with the retention of regional gradients and seasonal variability, provides a more complete observational representation of the spatial and temporal behaviour of atmospheric CO_2 over China.

Several limitations should be addressed in future work. First, broader independent validation is required, including additional TCCON stations and spatially or temporally blocked validation strategies. Second, the treatment of cross-platform retrieval differences and posterior uncertainty calibration should be further refined. Third, the physical representation of sensor-specific observation support, particularly for active lidar observations and under complex cloud or aerosol conditions, requires additional investigation. Future extensions may incorporate atmospheric transport constraints and apply the framework to other greenhouse and trace gases. Overall, PGO-BME provides a promising physically informed and uncertainty-aware approach

https://doi.org/10.5194/egusphere-2026-5998
Preprint. Discussion started: 10 November 2026
© Author(s) 2026. CC BY 4.0 License.

for multi-source satellite XCO_2 reconstruction and regional carbon monitoring. By improving the spatial continuity and uncertainty characterization of heterogeneous satellite XCO_2 observations, the framework provides a more reliable observational basis for examining regional atmospheric CO_2 variability and its spatial and temporal behaviour.

Code and data availability

The multi-source satellite fusion data generated in this study are available upon request. The primary datasets used in this study are obtained from the following sources: OCO-2 / OCO-3 XCO_2 data: Available from the NASA Goddard Earth Sciences Data and Information Services Center (GES DISC), product versions OCO2_L2_Lite_FP 11r and OCO3_L2_Lite_FP 11r. Data access: https://disc.gsfc.nasa.gov/datasets (last access: September 2024). GOSAT XCO_2 data: Available from the National Institute for Environmental Studies (NIES), Japan, product version TANSO-FTS SWIR Level 2 V03.05. Data access: https://data2.gosat.nies.go.jp/index_en.html (last access: September 2024).DQ-1 (Daqi-1) ACDL XCO_2 data: The orbital observations acquired by the ACDL payload were obtained through research collaboration. TCCON ground-based validation data: Available from the official TCCON data portal, version GGG2020. Data access: https://tccondata.org (last access: September 2025). In addition, auxiliary datasets used in this study (e.g., CAMS reanalysis products) are publicly available from their respective sources. All processed data and codes are available from the corresponding authors upon reasonable request.

Author contributions

HL: Conceptualization, Methodology, Data curation, Formal analysis, Investigation, Visualization, Writing (original draft preparation). QH: Conceptualization, Methodology, Investigation, Formal analysis, Validation, Writing (review and editing). SW: Conceptualization, Methodology, Supervision, Project administration, Funding acquisition, Writing (review and editing). KQ: Methodology, Supervision, Project administration, Funding acquisition, Writing (review and editing). JBC: Methodology, Validation, Interpretation of results, Writing (review and editing). YF: Data curation, Formal analysis, Visualization, Writing (review and editing). HG: Investigation, Validation, Visualization, Writing (review and editing). ZQL: Resources, Validation, Writing (review and editing). YB: Resources, Validation, Writing (review and editing). LZ: Resources, Validation, Writing (review and editing). All authors reviewed and approved the final manuscript.

Competing interests

Editorship CI! The authors have the following competing interests: At least one of the (co-)authors is a member of the editorial board of Atmospheric Chemistry and Physics.

https://doi.org/10.5194/egusphere-2026-5998
Preprint. Discussion started: 10 November 2026
© Author(s) 2026. CC BY 4.0 License.

Acknowledgements

The authors acknowledge the NASA Goddard Earth Sciences Data and Information Services Center (GES DISC) for providing the OCO-2 and OCO-3 XCO_2 products; the National Institute for Environmental Studies (NIES), Japan, for providing the GOSAT TANSO-FTS SWIR Level 2 V03.05 XCO_2 product; The DQ-1/ACDL orbital XCO_2 observations used in this study were obtained through scientific collaboration. We also acknowledge the TCCON science team and station operators for providing the GGG2020 ground-based observations, and the Copernicus Atmosphere Monitoring Service (CAMS) for providing the background fields used in this study.

Financial support

This work was supported by the Jing-Jin-Ji Regional Integrated Environmental Improvement–National Science and Technology Major Project of the Ministry of Ecology and Environment of China (No. 2025ZD1200900).

References

Bao, Y., Yang, Q., Yuan, Q., Hu, D., and Xu, Y.: Global Daily Atmospheric Methane Column Concentration Retrieval From TROPOMI Satellite Spectral Measurements by Two-Stage Machine Learning Algorithm, IEEE Journal of Selected Topics in Applied Earth Observations and Remote Sensing, 19, 15589-15607, 10.1109/JSTARS.2026.3688284, 2026.

Benoy, T., Wilson, D., Lengden, M., Armstrong, I., Stewart, G., and Johnstone, W.: Measurement of CO 2 concentration and temperature in an aero engine exhaust plume using wavelength modulation spectroscopy, IEEE Sensors Journal, 17, 6409-6417, 10.1109/JSEN.2017.2738333, 2017.

Buchwitz, M., Schneising, O., Burrows, J. P., Bovensmann, H., Reuter, M., and Notholt, J.: First direct observation of the atmospheric CO₂ year-to-year increase from space, Atmos. Chem. Phys., 7, 4249-4256, 10.5194/acp-7-4249-2007, 2007.

Byrne, B., Baker, D. F., Basu, S., Bertolacci, M., Bowman, K. W., Carroll, D., Chatterjee, A., Chevallier, F., Ciais, P., Cressie, N., Crisp, D., Crowell, S., Deng, F., Deng, Z., Deutscher, N. M., Dubey, M. K., Feng, S., García, O. E., Griffith, D. W. T., Herkommer, B., Hu, L., Jacobson, A. R., Janardanan, R., Jeong, S., Johnson, M. S., Jones, D. B. A., Kivi, R., Liu, J., Liu, Z., Maksyutov, S., Miller, J. B., Miller, S. M., Morino, I., Notholt, J., Oda, T., O'Dell, C. W., Oh, Y. S., Ohyama, H., Patra, P. K., Peiro, H., Petri, C., Philip, S., Pollard, D. F., Poulter, B., Remaud, M., Schuh, A., Sha, M. K., Shiomi, K., Strong, K., Sweeney, C., Té, Y., Tian, H., Velazco, V. A., Vrekoussis, M., Warneke, T., Worden, J. R., Wunch, D., Yao, Y., Yun, J., Zammit-Mangion, A., and Zeng, N.: National CO2 budgets (2015–2020) inferred from atmospheric CO2 observations in support of the global stocktake, Earth Syst. Sci. Data, 15, 963-1004, 10.5194/essd-15-963-2023, 2023.

Cao, X., Zhang, X., Zhang, L., Deng, Z., Zhang, L., Jiang, Y., Dou, H., Liu, J., and Fan, C.: Estimations of Wind Direction and CO2 Emissions From Power Plants With DaQi-1 Satellite, IEEE Transactions on Geoscience and Remote Sensing, 64, 1-16, 10.1109/TGRS.2026.3669000, 2026.

Chen, Y., Yuan, Q., Xie, H., Tang, Y., Xiao, Y., He, J., Guan, R., Liu, X., and Zhang, L.: Hyperspectral Video Tracking With Spectral-Spatial Fusion and Memory Enhancement, IEEE Trans Image Process, 34, 3547-3562, 10.1109/TIP.2025.3569479, 2025a.

Chen, Y. Z., Yuan, Q. Q., Xiao, Y., Tang, Y. Q., He, J., and Han, T.: STAR: A Unified Spatiotemporal Fusion Framework for Satellite Video Object Tracking, Ieee Transactions on Geoscience and Remote Sensing, 63, 1-1, Artn 5631122,10.1109/Tgrs.2025.3585112, 2025b.

https://doi.org/10.5194/egusphere-2026-5998
Preprint. Discussion started: 10 November 2026
© Author(s) 2026. CC BY 4.0 License.

Cheng, C. H., Liu, D., Wang, S. B., Zhang, X. Y., Zhang, L., Chen, W. B., Liu, J. Q., Wan, X. P., Chen, W. T., Chen, X. L., Zhang, J. X., Deng, J. S., Xu, W. T., Wu, L., Liu, C., and Xiang, Z.: Estimating strong point CO2 emissions by combining spaceborne IPDA lidar and HSRL, Remote Sensing of Environment, 328, 114898, ARTN 114898 10.1016/j.rse.2025.114898, 2025.

Christakos, G.: A Bayesian/maximum-entropy view to the spatial estimation problem, Mathematical Geology, 22, 763-777, https://doi.org/10.1007/BF00890661, 1990.

Christakos, G. and Li, X.: Bayesian Maximum Entropy Analysis and Mapping: A Farewell to Kriging Estimators?, Mathematical Geology, 30, 435-462, 10.1023/A:1021748324917, 1998.

Crisp, D., Pollock, H. R., Rosenberg, R., Chapsky, L., Lee, R. A. M., Oyafuso, F. A., Frankenberg, C., O'Dell, C. W., Bruegge, C. J., Doran, G. B., Eldering, A., Fisher, B. M., Fu, D., Gunson, M. R., Mandrake, L., Osterman, G. B., Schwandner, F. M., Sun, K., Taylor, T. E., Wennberg, P. O., and Wunch, D.: The on-orbit performance of the Orbiting Carbon Observatory-2 (OCO-2) instrument and its radiometrically calibrated products, Atmos. Meas. Tech., 10, 59-81, 10.5194/amt-10-59-2017, 2017.

Crisp, D., Atlas, R. M., Breon, F. M., Brown, L. R., Burrows, J. P., Ciais, P., Connor, B. J., Doney, S. C., Fung, I. Y., Jacob, D. J., Miller, C. E., O'Brien, D., Pawson, S., Randerson, J. T., Rayner, P., Salawitch, R. J., Sander, S. P., Sen, B., Stephens, G. L., Tans, P. P., Toon, G. C., Wennberg, P. O., Wofsy, S. C., Yung, Y. L., Kuang, Z., Chudasama, B., Sprague, G., Weiss, B., Pollock, R., Kenyon, D., and Schroll, S.: The Orbiting Carbon Observatory (OCO) mission, Advances in Space Research, 34, 700-709, https://doi.org/10.1016/j.asr.2003.08.062, 2004.

de Graaf, M., Sihler, H., Tilstra, L. G., and Stammes, P.: How big is an OMI pixel?, Atmospheric Measurement Techniques, 9, 3607-3618, 10.5194/amt-9-3607-2016, 2016.

Dou, X., Wang, Y., Ciais, P., Chevallier, F., Davis, S. J., Crippa, M., Janssens-Maenhout, G., Guizzardi, D., Solazzo, E., Yan, F., Huo, D., Zheng, B., Zhu, B., Cui, D., Ke, P., Sun, T., Wang, H., Zhang, Q., Gentine, P., Deng, Z., and Liu, Z.: Near-real-time global gridded daily CO2 emissions, The Innovation, 3, 100182, https://doi.org/10.1016/j.xinn.2021.100182, 2022.

Ehret, G., Kiemle, C., Wirth, M., Amediek, A., Fix, A., and Houwrling, S.: Space-borne remote sensing of CO2, CH4, and N 2O by integrated path differential absorption lidar: A sensitivity analysis, Applied Physics B, 90, 593-608, 10.1007/s00340-007-2892-3, 2008.

Eldering, A., Taylor, T. E., O'Dell, C. W., and Pavlick, R.: The OCO-3 mission: measurement objectives and expected performance based on 1 year of simulated data, Atmospheric Measurement Techniques, 12, 2341-2370, 10.5194/amt-12-2341-2019, 2019.

Friedlingstein, P., O'Sullivan, M., Jones, M. W., Andrew, R. M., Hauck, J., Landschützer, P., Le Quéré, C., Li, H., Luijkx, I. T., Olsen, A., Peters, G. P., Peters, W., Pongratz, J., Schwingshackl, C., Sitch, S., Canadell, J. G., Ciais, P., Jackson, R. B., Alin, S. R., Arneth, A., Arora, V., Bates, N. R., Becker, M., Bellouin, N., Berghoff, C. F., Bittig, H. C., Bopp, L., Cadule, P., Campbell, K., Chamberlain, M. A., Chandra, N., Chevallier, F., Chini, L. P., Colligan, T., Decayeux, J., Djeutchouang, L. M., Dou, X., Duran Rojas, C., Enyo, K., Evans, W., Fay, A. R., Feely, R. A., Ford, D. J., Foster, A., Gasser, T., Gehlen, M., Gkritzalis, T., Grassi, G., Gregor, L., Gruber, N., Gürses, Ö., Harris, I., Hefner, M., Heinke, J., Hurtt, G. C., Iida, Y., Ilyina, T., Jacobson, A. R., Jain, A. K., Jarníková, T., Jersild, A., Jiang, F., Jin, Z., Kato, E., Keeling, R. F., Klein Goldewijk, K., Knauer, J., Korsbakken, J. I., Lan, X., Lauvset, S. K., Lefèvre, N., Liu, Z., Liu, J., Ma, L., Maksyutov, S., Marland, G., Mayot, N., McGuire, P. C., Metzl, N., Monacci, N. M., Morgan, E. J., Nakaoka, S. I., Neill, C., Niwa, Y., Nützel, T., Olivier, L., Ono, T., Palmer, P. I., Pierrot, D., Qin, Z., Resplandy, L., Roobaert, A., Rosan, T. M., Rödenbeck, C., Schwinger, J., Smallman, T. L., Smith, S. M., Sospedra-Alfonso, R., Steinhoff, T., Sun, Q., Sutton, A. J., Séférian, R., Takao, S., Tatebe, H., Tian, H., Tilbrook, B., Torres, O., Tourigny, E., Tsujino, H., Tubiello, F., van der Werf, G., Wanninkhof, R., Wang, X., Yang, D., Yang, X., Yu, Z., Yuan, W., Yue, X., Zaehle, S., Zeng, N., and Zeng, J.: Global Carbon Budget 2024, Earth Syst. Sci. Data, 17, 965-1039, 10.5194/essd-17-965-2025, 2025.

Gao, Z., Jiang, Y., He, J., Wu, J., and Christakos, G.: Comparing eight remotely sensed sea surface temperature products and Bayesian maximum entropy-based data fusion products, Spatial Statistics, 54, 100741, https://doi.org/10.1016/j.spasta.2023.100741, 2023.

Han, G., Xu, H., Gong, W., Liu, J., Du, J., Ma, X., and Liang, A.: Feasibility Study on Measuring Atmospheric CO2 in Urban Areas Using Spaceborne CO2-IPDA LIDAR, Remote Sensing, 10, 985, 10.3390/rs10070985, 2018.

https://doi.org/10.5194/egusphere-2026-5998
Preprint. Discussion started: 10 November 2026
© Author(s) 2026. CC BY 4.0 License.

Han, G., Huang, Y., Shi, T., Zhang, H., Li, S., Zhang, H., Chen, W., Liu, J., and Gong, W.: Quantifying CO2 emissions of power plants with Aerosols and Carbon Dioxide Lidar onboard DQ-1, Remote Sensing of Environment, 313, 114368, https://doi.org/10.1016/j.rse.2024.114368, 2024.

Han, G., Zhang, H., Huang, Y., Chen, W., Mao, H., Zhang, X., Ma, X., Li, S., Zhang, H., and Liu, J.: First global XCO2 observations fromspaceborne lidar: methodology and initial result, Remote Sensing of Environment, 330, 114954, https://doi.org/10.1016/j.rse.2025.114954, 2025.

He, J. and Kolovos, A.: Bayesian maximum entropy approach and its applications: a review, Stochastic Environmental Research and Risk Assessment, 32, 859-877, 10.1007/s00477-017-1419-7, 2018.

He, J., Chen, Y., Wu, J., Stow, D. A., and Christakos, G.: Space-time chlorophyll-a retrieval in optically complex waters that accounts for remote sensing and modeling uncertainties and improves remote estimation accuracy, Water Res, 171, 115403, 10.1016/j.watres.2019.115403, 2020a.

He, Z., Lei, L., Zhang, Y., Sheng, M., Wu, C., Li, L., Zeng, Z.-C., and Welp, L. R.: Spatio-Temporal Mapping of Multi-Satellite Observed Column Atmospheric CO2 Using Precision-Weighted Kriging Method, 10.3390/rs12030576, 2020b.

Helliker, B. R., Berry, J. A., Betts, A. K., Bakwin, P. S., Davis, K. J., Denning, A. S., Ehleringer, J. R., Miller, J. B., Butler, M. P., and Ricciuto, D. M.: Estimates of net CO2 flux by application of equilibrium boundary layer concepts to CO2 and water vapor measurements from a tall tower, Journal of Geophysical Research: Atmospheres, 109, https://doi.org/10.1029/2004JD004532, 2004.

Hu, K., Liu, Z., Shao, P., Ma, K., Xu, Y., Wang, S., Wang, Y., Wang, H., Di, L., Xia, M., and Zhang, Y.: A Review of Satellite-Based CO2 Data Reconstruction Studies: Methodologies, Challenges, and Advances, Remote Sensing, 16, 3818, 10.3390/rs16203818, 2024.

Inamdar, D., Kalacska, M., Leblanc, G., and Arroyo-Mora, J. P.: Characterizing and Mitigating Sensor Generated Spatial Correlations in Airborne Hyperspectral Imaging Data, Remote Sensing, 12, 641, 10.3390/rs12040641, 2020.

Inamdar, D., Kalacska, M., Darko, P. O., Arroyo-Mora, J. P., and Leblanc, G.: Spatial response resampling (SR2): Accounting for the spatial point spread function in hyperspectral image resampling, MethodsX, 10, 101998, https://doi.org/10.1016/j.mex.2023.101998, 2023.

Jiang, Y., Gao, Z., He, J., Wu, J., and Christakos, G.: Application and Analysis of XCO2 Data from OCO Satellite Using a Synthetic DINEOF–BME Spatiotemporal Interpolation Framework, Remote Sensing, 14, 4422, 10.3390/rs14174422, 2022.

Jin, X., Merchant, Z., and Sun, K.: Physics-Based Spatial Oversampling of TROPOMI NO(2) Observations to US Neighborhoods Reveals the Disparities of Air Pollution, Geohealth, 9, e2025GH001423, 10.1029/2025GH001423, 2025.

Kuai, L., Natraj, V., Shia, R.-L., Miller, C., and Yung, Y. L.: Channel selection using information content analysis: A case study of CO2 retrieval from near infrared measurements, Journal of Quantitative Spectroscopy and Radiative Transfer, 111, 1296-1304, https://doi.org/10.1016/j.jqsrt.2010.02.011, 2010.

Laughner, J. L., Toon, G. C., Mendonca, J., Petri, C., Roche, S., Wunch, D., Blavier, J. F., Griffith, D. W. T., Heikkinen, P., Keeling, R. F., Kiel, M., Kivi, R., Roehl, C. M., Stephens, B. B., Baier, B. C., Chen, H., Choi, Y., Deutscher, N. M., DiGangi, J. P., Gross, J., Herkommer, B., Jeseck, P., Laemmel, T., Lan, X., McGee, E., McKain, K., Miller, J., Morino, I., Notholt, J., Ohyama, H., Pollard, D. F., Rettinger, M., Riris, H., Rousogenous, C., Sha, M. K., Shiomi, K., Strong, K., Sussmann, R., Té, Y., Velazco, V. A., Wofsy, S. C., Zhou, M., and Wennberg, P. O.: The Total Carbon Column Observing Network's GGG2020 data version, Earth Syst. Sci. Data, 16, 2197-2260, 10.5194/essd-16-2197-2024, 2024.

Lee, J., Jeong, S., Kim, Y. J., Roh, S., Kim, J., and Jin, H.: Synergy of Multiple-Satellite Measurements to Fill the Gap of Global XCO2, Journal of Geophysical Research: Atmospheres, 130, e2024JD042809, https://doi.org/10.1029/2024JD042809, 2025.

Li, X., Jiang, S., Wang, X., Wang, T., Zhang, S., Guo, J., and Jiao, D.: XCO2 Super-Resolution Reconstruction Based on Spatial Extreme Random Trees, Atmosphere, 15, 440, 10.3390/atmos15040440, 2024.

Liu, W., Xue, Y., Ling, X., He, B., Li, C., and Han, L.: Simulation and analysis of CO2 concentration in China from 2009 to 2021 based on the WRF-Chem model, Atmospheric Research, 333, 108732, https://doi.org/10.1016/j.atmosres.2025.108732, 2026.

Lu, L., Cohen, J. B., Qin, K., Tiwari, P., Hu, W., Gao, H., and Zheng, B.: New Perspective on Using Observational Uncertainty to Improve Reliability of NOx Emissions Over Northern China, IEEE Transactions on Geoscience and Remote Sensing, 63, 1-15, 10.1109/TGRS.2025.3620116, 2025.

https://doi.org/10.5194/egusphere-2026-5998
Preprint. Discussion started: 10 November 2026
© Author(s) 2026. CC BY 4.0 License.

Oshchepkov, S., Bril, A., Yokota, T., Wennberg, P. O., Deutscher, N. M., Wunch, D., Toon, G. C., Yoshida, Y., O'Dell, C. W., Crisp, D., Miller, C. E., Frankenberg, C., Butz, A., Aben, I., Guerlet, S., Hasekamp, O., Boesch, H., Cogan, A., Parker, R., Griffith, D., Macatangay, R., Notholt, J., Sussmann, R., Rettinger, M., Sherlock, V., Robinson, J., Kyrö, E., Heikkinen, P., Feist, D. G., Morino, I., Kadygrov, N., Belikov, D., Maksyutov, S., Matsunaga, T., Uchino, O., and Watanabe, H.: Effects of atmospheric light scattering on spectroscopic observations of greenhouse gases from space. Part 2: Algorithm intercomparison in the GOSAT data processing for CO2 retrievals over TCCON sites, Journal of Geophysical Research: Atmospheres, 118, 1493-1512, https://doi.org/10.1002/jgrd.50146, 2013.

Pan, G., Xu, Y., and Ma, J.: The potential of CO2 satellite monitoring for climate governance: A review, Journal of Environmental Management, 277, 111423, https://doi.org/10.1016/j.jenvman.2020.111423, 2021.

Qin, K., Gao, H., Liu, X., He, Q., Tiwari, P., and Cohen, J. B.: The global daily High Spatial–Temporal Coverage Merged tropospheric NO2 dataset (HSTCM-NO2) from 2007 to 2022 based on OMI and GOME-2, Earth Syst. Sci. Data, 16, 5287-5310, 10.5194/essd-16-5287-2024, 2024.

Qin, K., Lu, L., Liu, J., He, Q., Shi, J., Deng, W., Wang, S., and Cohen, J. B.: Model-free daily inversion of NOx emissions using TROPOMI (MCMFE-NOx) and its uncertainty: Declining regulated emissions and growth of new sources, Remote Sensing of Environment, 295, 113720, https://doi.org/10.1016/j.rse.2023.113720, 2023.

Reichstein, M., Bahn, M., Ciais, P., Frank, D., Mahecha, M. D., Seneviratne, S. I., Zscheischler, J., Beer, C., Buchmann, N., Frank, D. C., Papale, D., Rammig, A., Smith, P., Thonicke, K., van der Velde, M., Vicca, S., Walz, A., and Wattenbach, M.: Climate extremes and the carbon cycle, Nature, 500, 287-295, 10.1038/nature12350, 2013.

Shao, W., Yue, T., Zhang, L., Tian, W., Wang, H., Zhou, H., Wu, C., and Zhang, L.: Mapping daily 1-km resolution XCO2 in China using deep learning and multi-source data, Resources, Conservation and Recycling, 227, 108755, https://doi.org/10.1016/j.resconrec.2025.108755, 2026.

Sheng, M., Lei, L., Zeng, Z.-C., Rao, W., Song, H., and Wu, C.: Global land 1° mapping dataset of XCO2 from satellite observations of GOSAT and OCO-2 from 2009 to 2020, Big Earth Data, 7, 170-190, 10.1080/20964471.2022.2033149, 2023.

Sihler, H., Lübcke, P., Lang, R., Beirle, S., de Graaf, M., Hörmann, C., Lampel, J., Penning de Vries, M., Remmers, J., Trollope, E., Wang, Y., and Wagner, T.: In-operation field-of-view retrieval (IFR) for satellite and ground-based DOAS-type instruments applying coincident high-resolution imager data, Atmos. Meas. Tech., 10, 881-903, 10.5194/amt-10-881-2017, 2017.

Sun, K., Zhu, L., Cady-Pereira, K., Chan Miller, C., Chance, K., Clarisse, L., Coheur, P.-F., González Abad, G., Huang, G., Liu, X., Van Damme, M., Yang, K., and Zondlo, M.: A physics-based approach to oversample multi-satellite, multispecies observations to a common grid, Atmospheric Measurement Techniques, 11, 6679-6701, 10.5194/amt-11-6679-2018, 2018.

Tadić, J. M., Qiu, X., Miller, S., and Michalak, A. M.: Spatio-temporal approach to moving window block kriging of satellite data v1.0, Geosci. Model Dev., 10, 709-720, 10.5194/gmd-10-709-2017, 2017.

Tadić, J. M., Qiu, X., Yadav, V., and Michalak, A. M.: Mapping of satellite Earth observations using moving window block kriging, Geosci. Model Dev., 8, 3311-3319, 10.5194/gmd-8-3311-2015, 2015.

Tang, Q., Bo, Y., and Zhu, Y.: Spatiotemporal fusion of multiple-satellite aerosol optical depth (AOD) products using Bayesian maximum entropy method, Journal of Geophysical Research: Atmospheres, 121, 4034-4048, https://doi.org/10.1002/2015JD024571, 2016.

Taylor, T. E., O'Dell, C. W., Baker, D., Bruegge, C., Chang, A., Chapsky, L., Chatterjee, A., Cheng, C., Chevallier, F., Crisp, D., Dang, L., Drouin, B., Eldering, A., Feng, L., Fisher, B., Fu, D., Gunson, M., Haemmerle, V., Keller, G. R., Kiel, M., Kuai, L., Kurosu, T., Lambert, A., Laughner, J., Lee, R., Liu, J., Mandrake, L., Marchetti, Y., McGarragh, G., Merrelli, A., Nelson, R. R., Osterman, G., Oyafuso, F., Palmer, P. I., Payne, V. H., Rosenberg, R., Somkuti, P., Spiers, G., To, C., Weir, B., Wennberg, P. O., Yu, S., and Zong, J.: Evaluating the consistency between OCO-2 and OCO-3 XCO2 estimates derived from the NASA ACOS version 10 retrieval algorithm, Atmos. Meas. Tech., 16, 3173-3209, 10.5194/amt-16-3173-2023, 2023.

Wang, J.: Global daily 1 km gapless XCO_2 (2003−2023) derived from multi-satellite observations and a spatiotemporal deep learning framework, Environmental Impact Assessment Review, 117, 10.1016/j.eiar.2025.108146, 2026.

Wang, W., He, J., Feng, H., and Jin, Z.: High-Coverage Reconstruction of XCO(2) Using Multisource Satellite Remote Sensing Data in Beijing-Tianjin-Hebei Region, Int J Environ Res Public Health, 19, 10.3390/ijerph191710853, 2022.

Wang, Y., Yuan, Q., Li, T., Yang, Y., Zhou, S., and Zhang, L.: Seamless mapping of long-term (2010–2020) daily global XCO2 and XCH4 from the Greenhouse Gases Observing Satellite (GOSAT), Orbiting Carbon Observatory 2 (OCO-2), and CAMS global greenhouse gas reanalysis (CAMS-EGG4) with a spatiotemporally self-supervised fusion method, Earth Syst. Sci. Data, 15, 3597-3622, 10.5194/essd-15-3597-2023, 2023.

https://doi.org/10.5194/egusphere-2026-5998
Preprint. Discussion started: 10 November 2026
© Author(s) 2026. CC BY 4.0 License.

Wang, Z., Zhang, C., Shi, K., Shangguan, Y., Hu, B., Chen, X., Wei, D., Chen, S., Atkinson, P. M., and Zhang, Q.: A full-coverage satellite-based global atmospheric CO2 dataset at 0.05° resolution from 2015 to 2021 for exploring global carbon dynamics, Earth Syst. Sci. Data, 17, 5355-5375, 10.5194/essd-17-5355-2025, 2025.

Wu, C., Ju, Y., Yang, S., Zhang, Z., and Chen, Y.: Reconstructing annual XCO(2) at a 1 kmx1 km spatial resolution across China from 2012 to 2019 based on a spatial CatBoost method, Environ Res, 236, 116866, 10.1016/j.envres.2023.116866, 2023.

Xia, P., Zhang, L., Min, M., Li, J., Wang, Y., Yu, Y., and Jia, S.: Accurate nowcasting of cloud cover at solar photovoltaic plants using geostationary satellite images, Nature Communications, 15, 510, 10.1038/s41467-023-44666-1, 2024.

Xia, P., Deng, D., Yang, X., Chand, S. S., Min, M., Li, J., Xu, N., Meng, D., Yu, Q., and Zhou, R.: Satellite-Derived Upper-Level Vorticity as an Indicator of Short-Term Typhoon Intensity Evolution, AGU Advances, 7, e2026AV002688, https://doi.org/10.1029/2026AV002688, 2026.

Yuan, Q., Zhong, W., Yang, Q., Peng, Y., Bolch, T., Wang, Y., Yue, L., Shen, H., and Zhang, L.: Duration of frozen days show a strong decline in the Northern Hemisphere mainly driven by autumn temperature increase, The Innovation Geoscience, 3, 100118, 10.59717/j.xinn-geo.2024.100118, 2025.

Zhang, L., Li, T., and Wu, J.: Deriving gapless CO2 concentrations using a geographically weighted neural network: China, 2014–2020, International Journal of Applied Earth Observation and Geoinformation, 114, 10.1016/j.jag.2022.103063, 2022.

Zhang, L., Cheng, T., Yue, T., Li, S., and Wilson, J. P.: Quantitative analysis of spatiotemporal coverage and uncertainty decomposition in OCO-2/3 XCO2 across China, Atmospheric Environment, 333, 120636, https://doi.org/10.1016/j.atmosenv.2024.120636, 2024.